Hindawi
Geofluids
Volume 2022, Article ID 9727124, 13 pages
https://doi.org/10.1155/2022/9727124

Research Article

The Effect of Hydraulic Coupling on Mechanical Deformation Characteristics of Shallow Coal Seam in Western Mining Area

Chunwei Ling,[1,2] **Xiaoshan Shi**,[3] **Hao Wang**,[1,2] **Kangning Zhang**,[1,2] **Qingshan Ren**,[1,2] **and Yinghua Lv**[4]

[1]*Beijing Key Laboratory for Precise Mining of Intergrown Energy and Resources, China University of Mining and Technology (Beijing), Beijing 100083, China*
[2]*School of Energy and Mining Engineering, University of Mining and Technology (Beijing), Beijing 100083, China*
[3]*Deep Mining and Rock Burst Research Institute, China Coal Research institute, Beijing 100013, China*
[4]*Shenhua Shendong Coal Group Company Limited, Shenmu 719315, China*

Correspondence should be addressed to Xiaoshan Shi; shixiaoshan2020@163.com

Received 31 December 2021; Accepted 23 February 2022; Published 12 March 2022

Academic Editor: Dongdong Ma

During coal mining, the mechanical and deformation behavior of the overburden is affected by water and stress. Therefore, it is of great significance to study the mechanical behavior of the surrounding rock under the action of hydraulic coupling. For high-intensity mining with shallow coal seam and large mining and strong strata behavior in stope, the hydraulic support is often damaged. Based on basic experiments and physical similarity simulations, overburden fracture in shallow coal seam in western mining area under hydraulic coupling was studied. The results show that under the loading rate range of 0.5~5 mm/min, the compressive strength of sandstone increases with the loading rate. The faster the loading rate, the shorter the duration of the rock sample being loaded and damaged, and the fewer the acoustic emission events. The first weighting step of the main roof of the working face is 54 m, the periodic weighting step is 12.75~28 m, and the average periodic weighting step is 22 m. There are only caving zone and fractured zone in the overburden of working face; the height of caving zone and fractured zone is 60 m and 168 m, respectively. The strength of the saturated sample is significantly reduced. During the excavation of the working face, the temperature difference between the fracture and the overburden value is ≥1°C, which can be used as a threshold for judging the development range of overburden fracture in similar simulation experiments.

1. Introduction

With the shift of China coal resource strategy, a large number of modern large scale coal production bases represented by the Shendong mining area have emerged in Western China. Compared with the mining areas in the central and eastern regions, the coal deposits in this area are relatively shallow, the thickness of the coal seam is relatively large, and the overburden are mostly in a weakly cemented state [1–4]. And under the conditions of high-intensity advancing mining, more severe mine pressure manifestations and ground subsidence changes appear. As a result, the thin bedrock is broken to produce fracture that penetrates the ground and the working face, forming a water-sand inrush breaking channel, triggering mine disasters, and threatening production safety.

Currently, with the aid of numerical simulation, monitoring, theoretical analysis, and similar simulation methods, the structural damage and fracture evolution of the overburden with shallow coal seam and large mining height in the western mining area have been studied, which monitor the ground subsidence of the working face and the characteristics of the roof pressure and analyze the dynamic changes of the overburden [4–8]. When mining shallow and thin bedrock coal seams, the relationship between roof geological structure, mining space parameters, and roof stability was obtained [9–11]. Under the strong mining disturbance caused by high-intensity rapid mining to the migration of

overburden, the law of failure and migration of key stratum under the condition of shallow coal seam thin bedrock and large mining height was established. Based on the relationship between the thickness of the loose layer and the height of the collapse arch of the overburden, the mining method to reduce the surface subsidence and the strip mining and filling method are pointed out [12–15]. Overburden fractures in shallow coal seam and large mining height stope often occur during the slow mining speed period, which is similar to the failure characteristics of bedrock materials. The stress field of the overburden on the roof changes with time, which in turn affects the strength of the rock and the migration state of the overburden. Therefore, through the compressive strength of the rock specimen taken under different loading conditions, theoretical analysis, and field monitoring data, the failure characteristics of the overburden in shallow coal seam with large mining height are investigated [16–24]. Moreover, the overburden failure can be divided into two stages. Through the insufficiency mining and the full mining of the overburden fracture, combined with the relationship between the overburden fracture and the tensile deformation of the strata, with the help of the field monitoring data, the overburden is discussed. Prediction method for the development of fracture height in overburden was proposed [25–28]. The failure characteristics of rock materials under different loads are discussed. At the same time, through physical similarity to simulate field conditions, the overburden migration and evolution laws can be studied more intuitively fractal, and the evolution of overburden breaking spatial structure and the occurrence of roof dynamic disasters during the entire mining process are systematically studied [12, 29–35]. Most of the above is the study of the law of overburden fault development. However, reports on the evolution of overburden fractures in shallow coal seams with large mining heights through basic experiments of infrared monitoring physical simulation methods are limited.

Under the conditions of shallow coal seam, thin bedrock, and large high-intensity mining, there are a large mining space, a strong mining disturbance process, and an overburden cutting subsidence, and dynamic load impact characteristics are obvious. Therefore, this study is based on the Shangwan coal mine in the western mining area. It is necessary to combine infrared monitoring methods and indoor similar physical simulations to study the evolution law of overburden fractures in shallow coal seams with the large mining heights.

2. Project Background

2.1. Geological Conditions of Coal Seam Occurrence. As shown in Figure 1, the 12401 working face of Shangwan mine is the first fully mechanized coal face with ultralarge mining height in the Shendong mining area. There are multiple thick hard rock layers on the roof. The thickness is 7.95~9.25 m, with an average of 8.8 m, and the inclination angle of the coal seam is 1~3°, which is a stable to relatively stable coal seam. Most of the ground is covered by aeolian sand; the thickness of the loose layer and bedrock is 0~25 m and 52~246 m, respectively. The mine field is mostly covered by loose layers. The exposed part of the bedrock has been subjected to varying degrees of weathering and denudation for a long time. The shallow bedrock is loose and fragile, with low hardness, and the deep rock is dense and hard. The lithology of coal seam no. 1-2 is mainly sandy mudstone, siltstone, and local fine coarse sandstone, mudstone, and claystone. The rock is dense and hard and has good stability. The compressive strength of the roof and floor rocks of the main mineable coal seams is also relatively large, and the strength of the roof and floor rocks of the coal seams is hard, and relatively stable, which is not easy to cause roof collapse.

2.2. Characteristics of Mining pressure on Working Face. As shown in Figure 2(a), according to the thickness of the 1-2 seam in Shangwan coal mine, the mining height is 8.8 m, the hydraulic support is selected as ZY29000/43/92D, the support height is 9.2 m, and the minimum support height is 4.3 m. As shown in Figure 2(b), the spatial distribution characteristics of the support resistance during the working face advance, the roof pressure periodicity is obvious, and the periodic weighting distance is between 12 and 25 m. The support resistance shows the characteristics of large in the middle of the working face and small at both ends, affected by the main roof dynamic load impact; the local support resistance peak is obvious; the maximum load reaches 506 bar.

3. Laboratory Experiment

3.1. Mechanical Experiment. The test rock samples were taken from the roof of the 12401 working face of Shangwan coal mine. Since the core sample location is the Shendong mining area, the saturation of the sandstone rock samples is low, and the water saturation of the sandstone was not tested in the early stage. During the coring process, the samples were only stored with plastic films. The experimental plan is to perform uniaxial compression tests under different loading rates. There are 3 sets of sandstone rock samples with 3 samples in each group, and there are 9 cylindrical rock samples in total. Field measurements analyze the characteristics of the coal mine static and dynamic loads. The monitoring results show that the dynamic load strain rate of coal mine mining is generally less than 10^{-1} s^{-1}, and the strain rate near the mine seismic source is 10^{-3}~10^{-1} s^{-1} [36–38]. Therefore, the stress disturbance range of coal mining is 10-5 s^{-1}~10^{-3} s^{-1}. This article set displacement loading rate is 0.5 mm/min, 1 mm/min, and 5 mm/min, and the corresponding strain rate is 8.3×10^{-5} s^{-1}, 1.6×10^{-4} s^{-1}, and 8.3×10^{-4} s^{-1}. Representative and better samples from the rock samples of this test for analysis are selected, as shown in Table 1. Figure 3(a) shows the experimental equipment. The testing equipment mainly includes the testing machine MTS universal testing machine, the maximum load is 300 kN, and the load displacement range is 0.001~254 mm/min. The monitoring equipment has a multichannel PCI-Express 8 acoustic emission monitor, and the sensor size is $\varphi 8 \times 8$ mm. Using the 16-channel strain acquisition instrument, the acquisition frequency is 1 MHz. Figure 3(b) shows

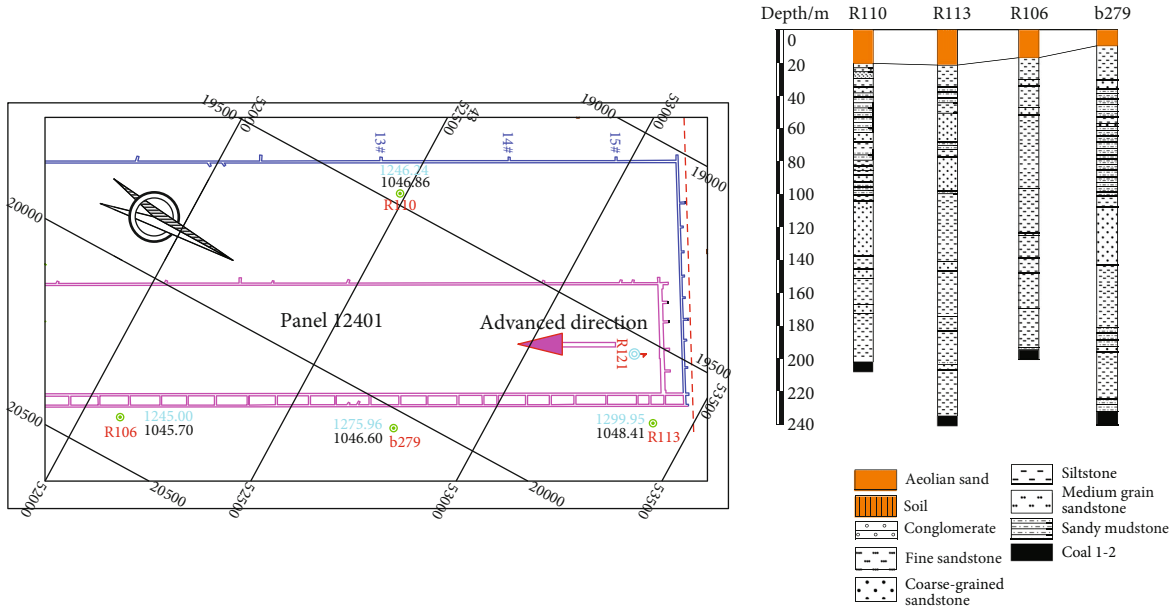

(a) (b)

Figure 1: Working face and histogram.

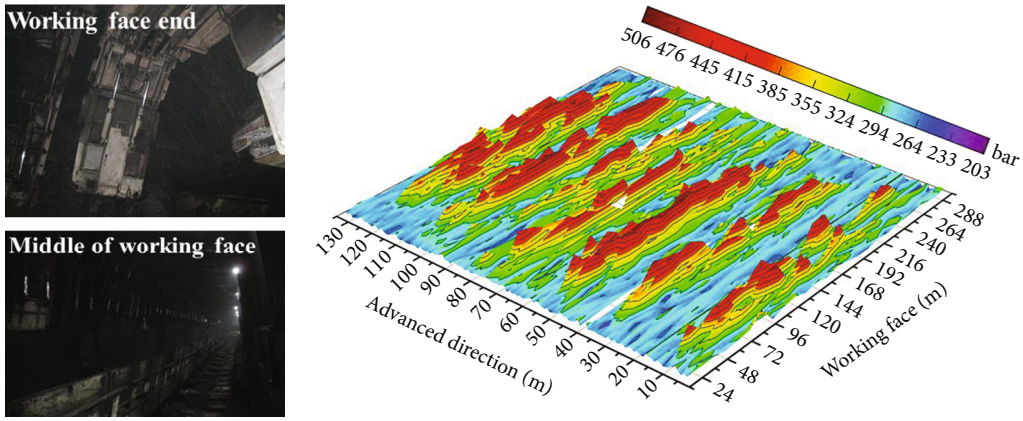

(a) (b)

Figure 2: Characteristics of mine pressure: (a) working face position and (b) spatial distribution of support resistance.

Table 1: Physical and mechanical parameters of sandstone under uniaxial compression.

Sample no.	Diameter (mm)	Height (mm)	Density (g/cm^3)	Loading rate (mm/min)	Compressive strength (MPa)	Mean (MPa)	E (GPa)	Mean (GPa)
S-12	48.76	100.07	2.38	0.5	43.33		5.55	
S-22	49.11	100.66	2.36	1	55.22	51.45	6.16	5.86
S-32	49.13	100.34	2.38	5	55.82		5.88	

the arrangement of AE sensors. The acoustic emission sensors are arranged 15 cm away from the two ends of the rock sample, and Vaseline was used as the couplant. The strain gauges are arranged in the middle of the rock sample. Figure 4 shows the failure modes of rock specimens under different loading rates. Under continuous uniaxial loading, the rock specimens occurred multiple fracture cracks, accompanying with "X"-shaped failures.

3.2. Model Physical Parameters. In order to obtain the characteristics of the migration and breaking of the overburden of the thick coal seam, the geological conditions of the

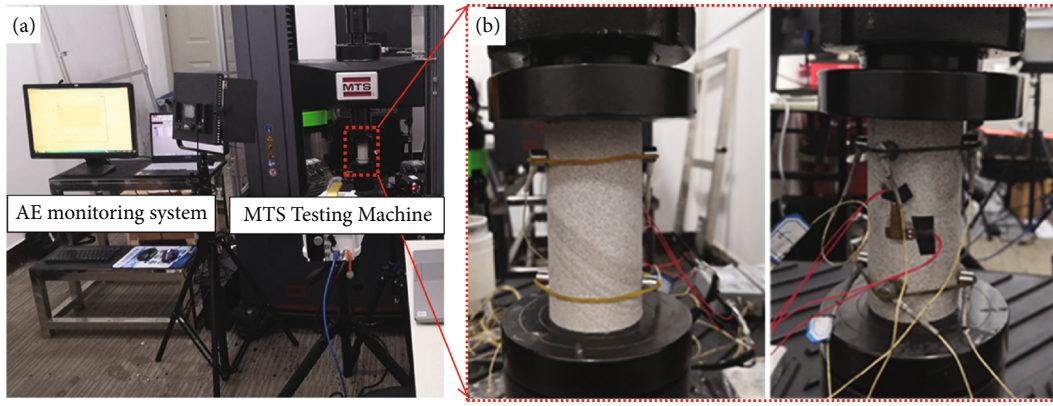

Figure 3: Test system: (a) experimental equipment and (b) arrangement of AE sensors.

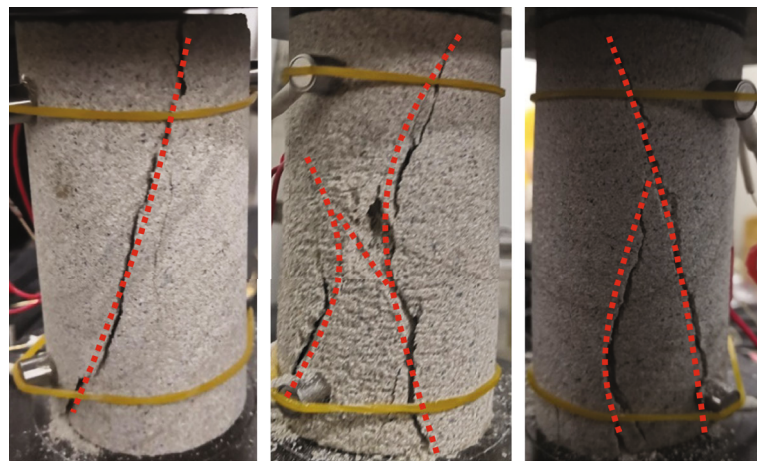

Figure 4: Failure characteristic of rock specimen under uniaxial.

Shangwan coal mine in this simulation experiment are used as a prototype. The simulated coal seam depth is 220 m, and the coal seam thickness is 8 m. As shown in Figure 5, the dimension of the model was $180 \times 20 \times 120$ cm (length × height × thickness). Based on similarity theory and previous related research [6, 15, 34, 35], it is determined that the geometric similarity ratio is 200 : 1 and the bulk density similarity ratio is 1.5 : 1. The simulation material uses river sand, calcium carbonate, and gypsum as materials, uses mica as auxiliary materials, and adds a certain proportion of fly ash to the coal seam. The final determination of the physical similarity simulation material ratio is shown in Table 2. The model only considers the weight of the overburden, leaving 20 cm coal pillars on both sides to eliminate the boundary effect. The main equipment used in the similar simulation experiment is shown in Figures 5(b) and 5(c).

3.3. Overburden Collapse Morphology Characteristics. As shown in Figure 6, the open cut is set at a distance of 40 m from the boundary. When the working face is advanced to 80 m, the main roof collapses, the roof hanging distance is 50 m, and the collapse height is 32 m. The collapsed shape is trapezoidal. Because the lithology of the main roof is relatively hard, it is not easy to collapse, resulting in a large collapse step. When the working face is advanced to 120 m, the main roof collapsed again, the roof hanging distance is 68 m, the collapsed height is 37 m, and basically, the roof did not break. When the working face advances to 160 m, the main roof collapses, the roof hanging distance is 96 m, and the collapse height is 100 m. The main roof is broken, and separation fracture appears in the overburden above the main roof. However, no supporting structure was formed but collapsed into the goaf along with the fracture angle of the rock. As the working face advances, the space of the goaf increases, and when the overburden reaches the limit span, the overburden breaks and fills the goaf. Due to the trapezoidal collapse space of the overburden, the roof hanging distance of the overburden gradually becomes smaller as the strata level rises. When the working face is advanced to 200 m, the roof hanging distance is 110 m, the collapse height is 100 m, and the main roof overburden fractured rock blocks are arranged in an orderly manner. The overburden fracture expands, the main roof is periodically broken, and the developed fracture expands to the main roof interface and penetrates the main roof to form fracture, which weaken the load capacity of the main roof cantilever beam. When the working face advances to 240 m, the main key stratum is broken, the roof hanging distance is 104 m, and

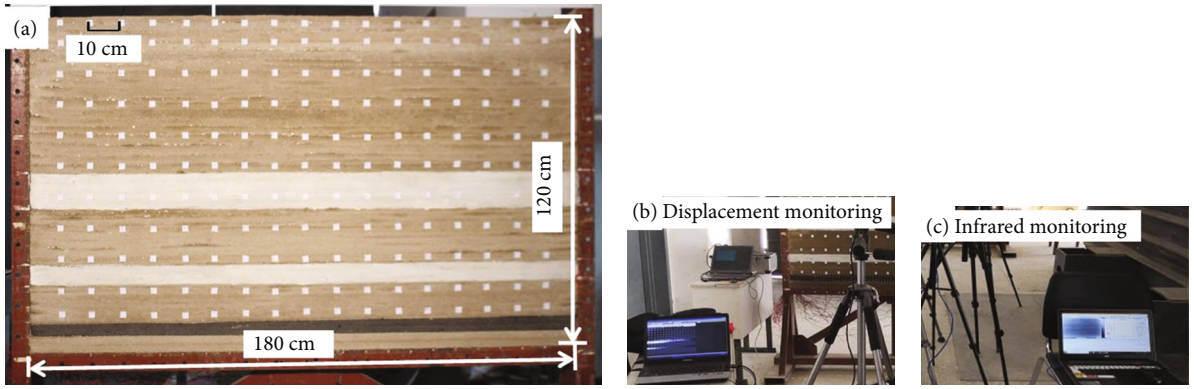

(a) (b) (c)

Figure 5: Physical model and measuring equipment.

Table 2: Material ratio of physical similarity model.

Lithology	Cumulative thickness (cm)	Sand (kg)	Lime (kg)	Plaster (kg)	Water (kg)
Aeolian sand	120.0	9.9	1.9	0.5	0.9
Siltstone	105.5	1.9	0.4	0.4	0.2
Fine-grained sandstone	105.0	11.6	3.8	3.9	1.4
Coarse-grained sandstone	94.5	6.6	0.9	0.7	0.6
Sandy mudstone	93.0	10.3	2.2	2.2	1.1
Medium-grained sandstone	85.0	11.6	2.4	2.5	1.2
Coarse-grained sandstone	82.0	4.4	0.6	0.4	0.4
Sandy mudstone	81.0	11.9	2.5	2.5	1.2
Fine-grained sandstone	62.5	8.3	2.7	2.7	0.9
Coarse-grained sandstone	60.0	13.2	1.9	1.3	1.2
Coarse-grained sandstone	57.0	9.5	3.1	3.2	1.19
Medium-grained sandstone	45.5	3.9	0.8	0.8	0.4
Sandy mudstone	44.5	5.8	1.2	1.2	0.6
Coarse-grained sandstone	43.0	9.9	1.4	0.9	0.9
Sandy mudstone	38.5	10.6	2.2	2.3	1.1
Fine-grained sandstone	27.5	7.7	2.5	2.6	0.9
Sandy mudstone	20.5	5.8	1.2	1.2	0.6
Siltstone	19.0	11.6	3.8	3.9	1.4
Sandy mudstone	15.5	3.9	0.8	0.8	0.4
Fine-grained sandstone	14.5	6.6	2.2	2.2	0.8
Mudstone	10.5	4.4	0.6	0.4	0.4
Coal 1-2	9.0	9.9	1.7	0.7	0.9
Mudstone	5.0	8.3	2.7	2.8	0.9

the collapse height is 168 m. The overburden fracture expanded upward, the main key stratum was broken, and the overburden of the main key stratum only produced separation fracture, and the vertical cracks did not penetrate to the surface. When the working face advances to 280 m, the main key stratum and overburden break sink. With the simultaneous subsidence of the ground surface, the fracture extends to the ground surface, and the ground collapses to form a sinking basin. The lateral distance of the basin is 100 m, and the central subsidence value is 5 m, and the collapse height is 228 m.

3.4. Temperature Field Characteristics of Overburden Fracture. As shown in Figure 7, the infrared camera is used to monitor simulation experiments. When measuring temperature, set the emissivity of the infrared camera to be the same as the emissivity value of the material to be measured, so that the measured value is consistent with the real temperature of the measured object. Therefore, before starting the monitoring, use a thermometer to monitor the temperature of the measured object in the room, compare it with the temperature measured by the infrared camera, and then perform calibration. From the temperature field distribution of

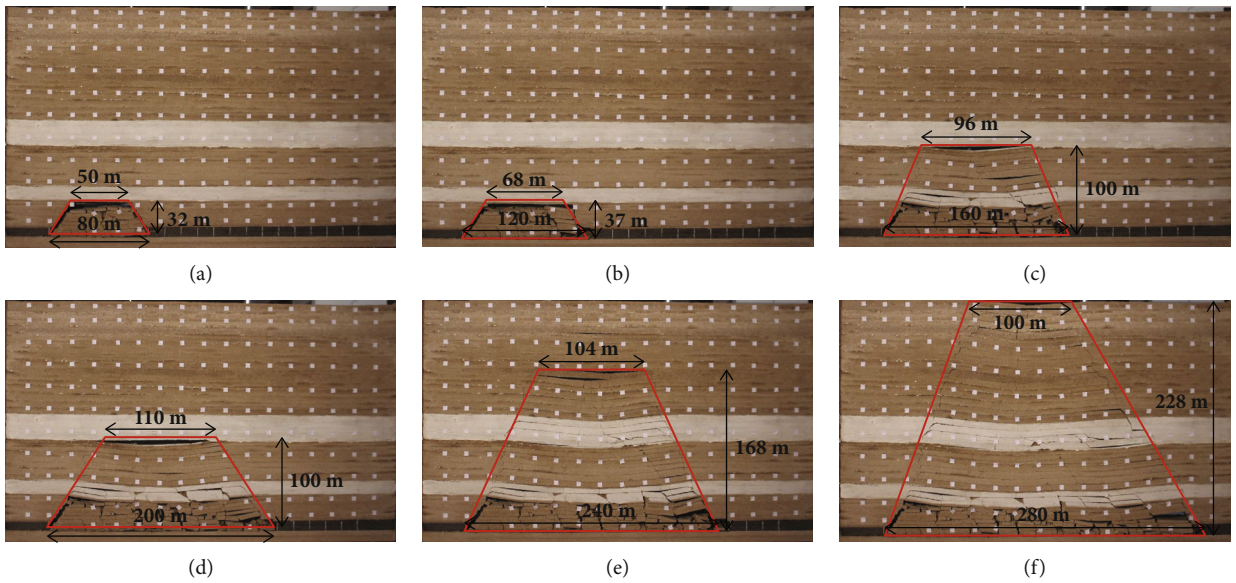

Figure 6: Evolution characteristics of overburden fracture during advancing of shallow working face.

the overburden fracture, it can be concluded that the temperature of the unbroken overburden remains basically stable during the working face advance process. The temperature distribution range of the overburden fracture zone is 4.14~19.63°C, and the temperature difference is 15.49°C. When the working face advances from 80 m to 120 m, the temperature field in the overburden fracture zone increases slightly. When the working face advances to 160 m, the temperature field increases in the overburden fracture zone. When the working face is advanced to 200 m, the overburden fracture expands, and the temperature increase range formed increases with the overburden fracture range. Because the separation fracture has indoor air entering, the overburden fracture temperature range is close to room temperature. When the working face advances to 240 m, the overburden fracture expansion range increases, the increasing temperature range increases, and the fracture zone is compacted. The temperature in the compaction zone is lower than the temperature in the fracture zone of the overburden. When the working face advances to 280 m, the overburden of the key stratum is bent and compacted, and the temperature change range is not increased. The overburden fracture zone under the key stratum is squeezed. The temperature change range is lower than the temperature value when the working face advances 240 m.

4. Results and Discussion

4.1. Deformation and Failure Characteristics of Roof Sandstone. Figure 8 shows the stress-strain curves of typical rock samples under different loading rates. It is concluded that the deformation and failure characteristics of the rock samples under different loading rates are basically the same [39–41]. In the initial stage of loading, the rock sample is the primary fracture compaction stage. The internal pores and fractures are compacted and closed under the external load, resulting in the rate of deformation greater than the rate of load, and the upward concave curve shows nonlinear characteristics. The load gradually increases, and the curve presents an approximate linear shape. This stage is a linear elastic stage, and a few microcracks are generated inside the rock sample. The curve presents an upward convex shape. This stage is the plastic stage. A large number of cracks have sprouted inside the rock sample, and some of the cracks are connected to each other. When the maximum peak load is reached, macroscopic cracks are formed on the surface of the rock sample, the rock sample is fractured instantaneously, and the stress value drops suddenly. As the loading rate increases, the proportion of the compaction stage in the prepeak stage decreases. The reason is that as the loading rate increases, the rate of the input energy absorbed by the rock sample increases, and the rate of closure of the internal pores and cracks in the rock sample increases, which ultimately results in the shortening of the compaction stage. In the loading rate range of 0.5~5 mm/min, the compressive strength of sandstone increases with the loading rate. Therefore, the mining speed will affect the development of fractures in the overburden.

By determining the location of the acoustic emission (AE) event, it can reflect the internal crack propagation and evolution law of the sample to a certain extent. Figure 9 shows the AE events of the spatial evolution of sandstone under different loading rate. The spatial evolution law of rock samples under different loading rates is basically the same. The crack compaction stage is the initial stage of loading. The original defects such as internal cracks and pores in the rock sample are gradually compacted and closed, and only a small number of acoustic emission events are generated, and the amplitude range is 40~90 dB. During the crack initiation stage, a small amount of cracks began to occur inside the rock sample, and only a small amount of acoustic emission events were generated, and the amplitude range was 40~90 dB. In the stage of stable crack propagation, the internal cracks of the rock sample develop faster and

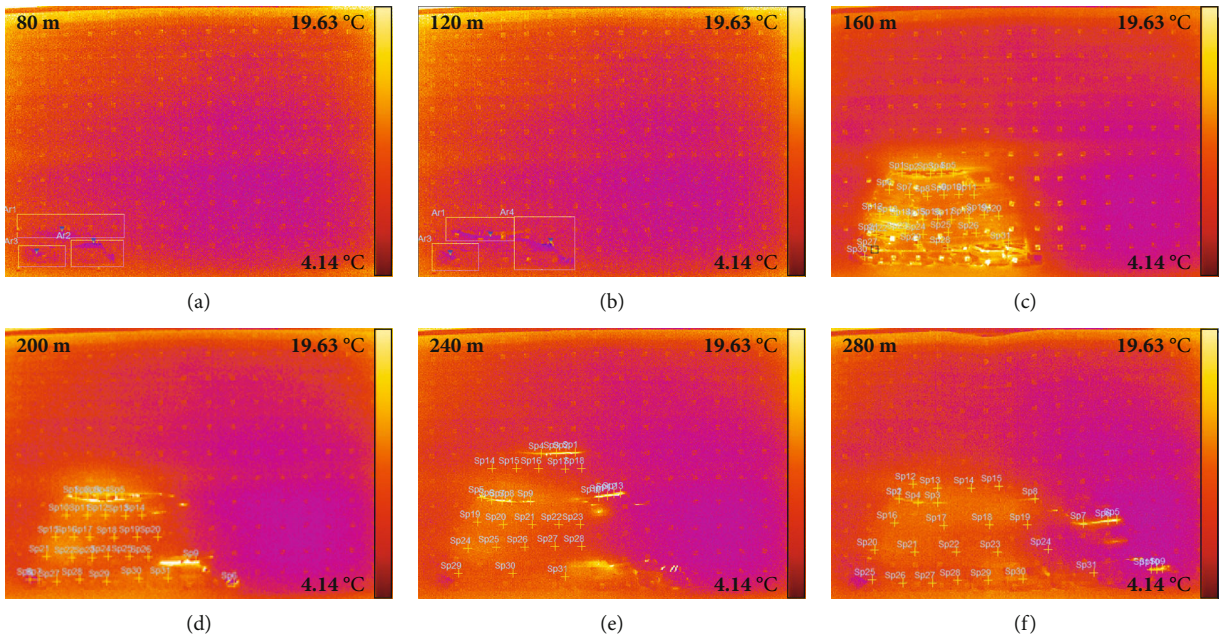

Figure 7: Evolution characteristics of overburden temperature field during advancing of working face.

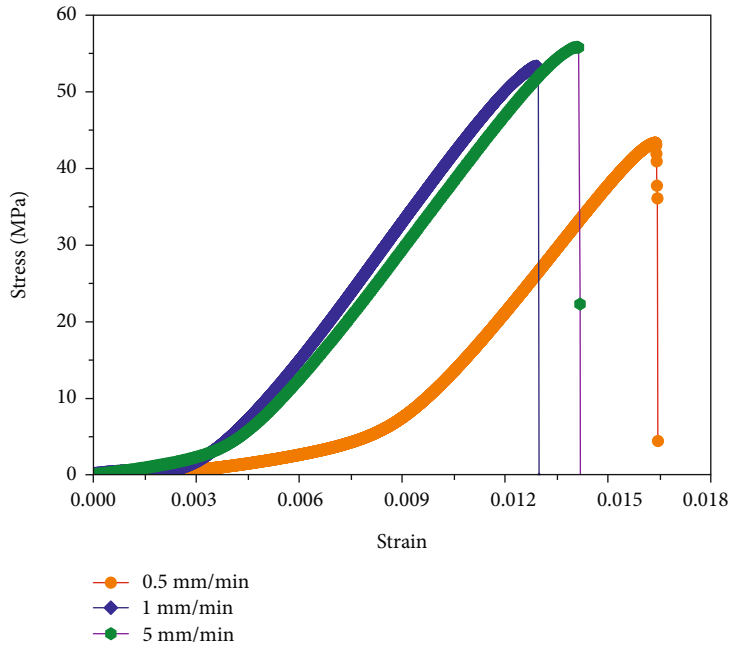

Figure 8: The curves of stress-strain under uniaxial.

produce more acoustic emission events, and the amplitude ranges from 40 to 100 dB. The postpeak failure stage is when the load exceeds the peak load. Due to the instantaneous fracture of the rock sample, some acoustic emission sensors fall off, and only a small amount of acoustic emission is detected.

During the entire loading process, the acoustic emission events were concentrated in the middle of the rock sample, indicating that the damage of the rock sample was concentrated in the middle of the sample. When the rock sample is finally destroyed, there are more acoustic emission events at a loading rate of 0.5 mm/min than at 1 mm/min and 5 mm/min. It shows that the faster the loading rate, the shorter the duration of the rock sample being loaded and destroyed, and the fewer the acoustic emission events.

In many studies, in the process of rock deformation and failure, different cracks in the rock generate corresponding different types of acoustic emission signals, which are generally divided into tension cracks, shear cracks, and tension-shear mixed cracks. Tension cracks can be represented by waveforms with lower RA values and higher AF values, and shear cracks can be represented by waveforms with

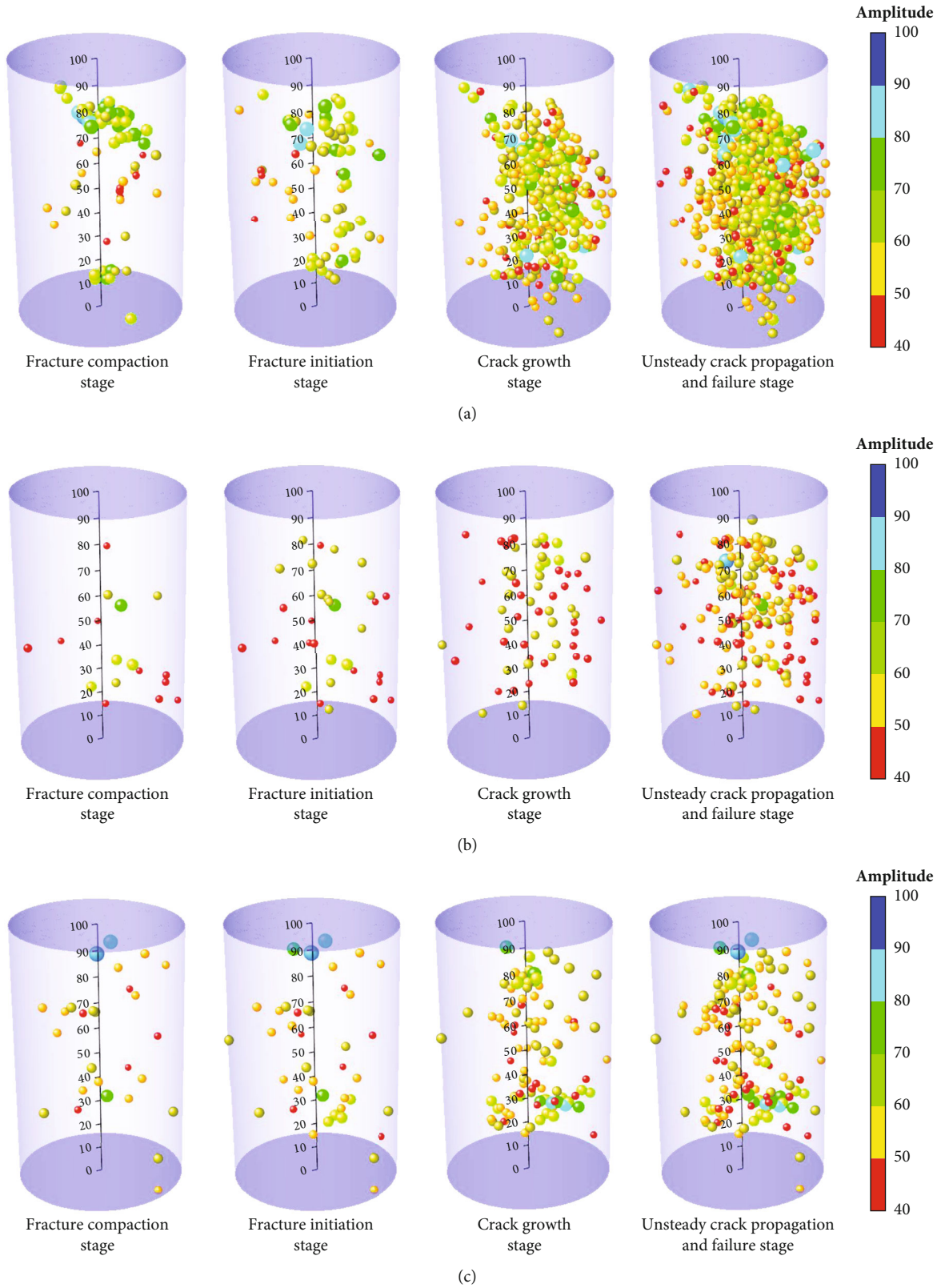

Figure 9: AE events of the spatial evolution of sandstone under different loading rate: (a) 0.5 mm/min, (b) 1 mm/min, and (c) 5 mm/min.

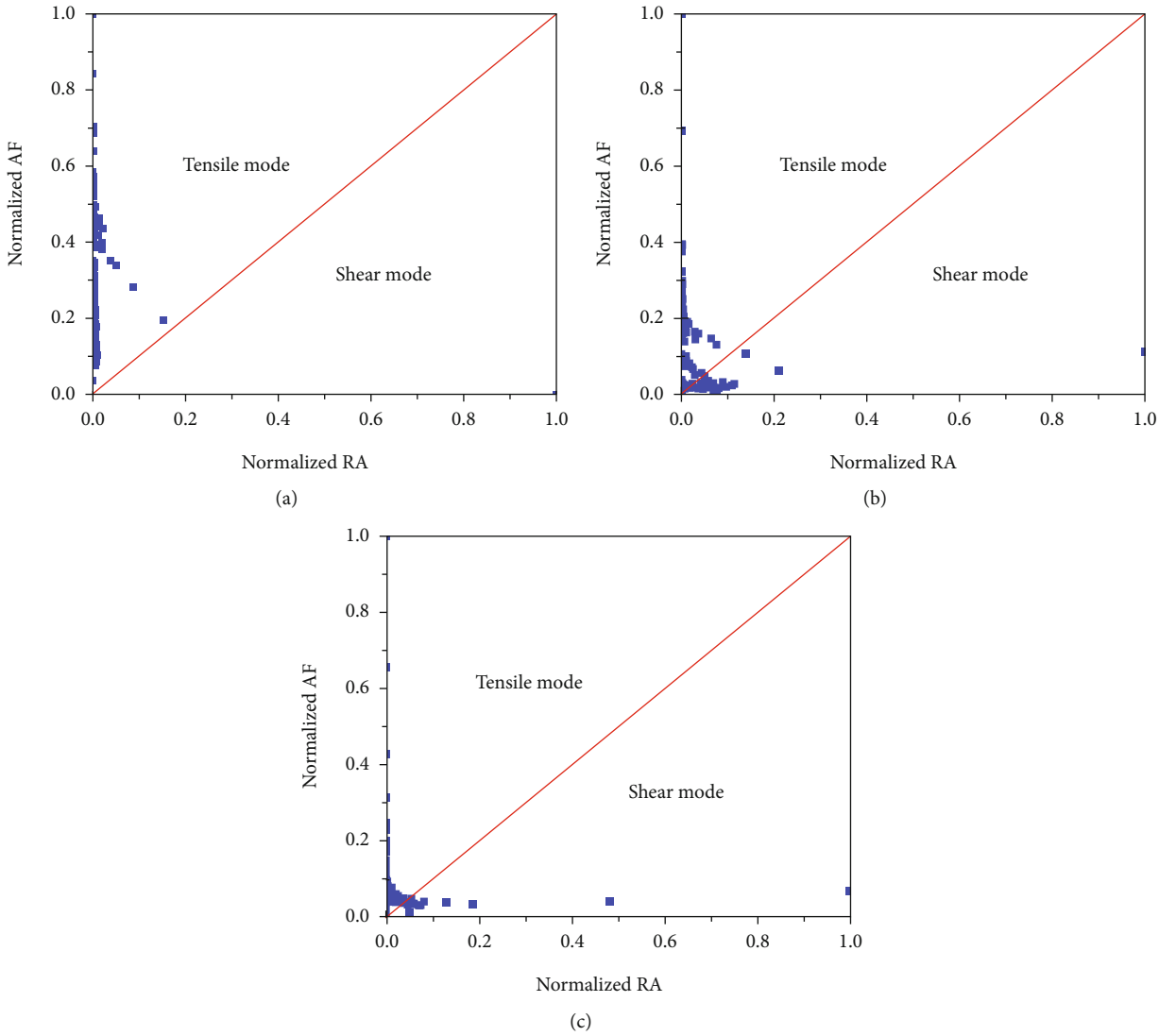

Figure 10: Distribution of RA-AF values in granite at different strain rates under uniaxial compression test: (a) 0.5 mm/min, (b) 1 mm/min, and (c) 5 mm/min.

higher RA values and lower AF values, where the RA value is the difference between the rise time and the amplitude Ratio, AF value is the ratio of count to duration. Calculate the RA value and AF value of the acoustic emission signal time series parameters of the sandstone sample under different loading rates. In order to eliminate the difference of different parameter dimensions, the RA-AF value is normalized, and the linear function normalization can ensure that the sample data reflects the original data. The distribution form makes the calculation result fall into the interval [0, 1], normalized and formulated as follows:

$$X_n = \frac{X - X_{\min}}{X_{\max} - X_{\min}}, \quad (1)$$

where X_n is the n-th normalized data of each parameter; X_n is the n-th data of each parameter; and $X_{\max}$ and $X_{\min}$ are the maximum and minimum values of each parameter.

Figure 10 shows the distribution of RA-AF values in granite at different strain rates under uniaxial compression test. The analysis shows that the distribution range of the AF-RA value of the rock samples under different loading rates is basically the same. The AF-RA data density range is large, mainly distributed near the vertical axis. The RA value is small, and the AF and RA values at the coordinate points are both small. Only a small amount is distributed near the horizontal axis, indicating the rock samples under different loading rates. The microscopic failure mechanism is mainly tensile failure, accompanied by a small amount of shear failure and mixed tension and shear failure. However, the AF-RA distribution of rock samples has a certain difference under different loading rates. With the increase

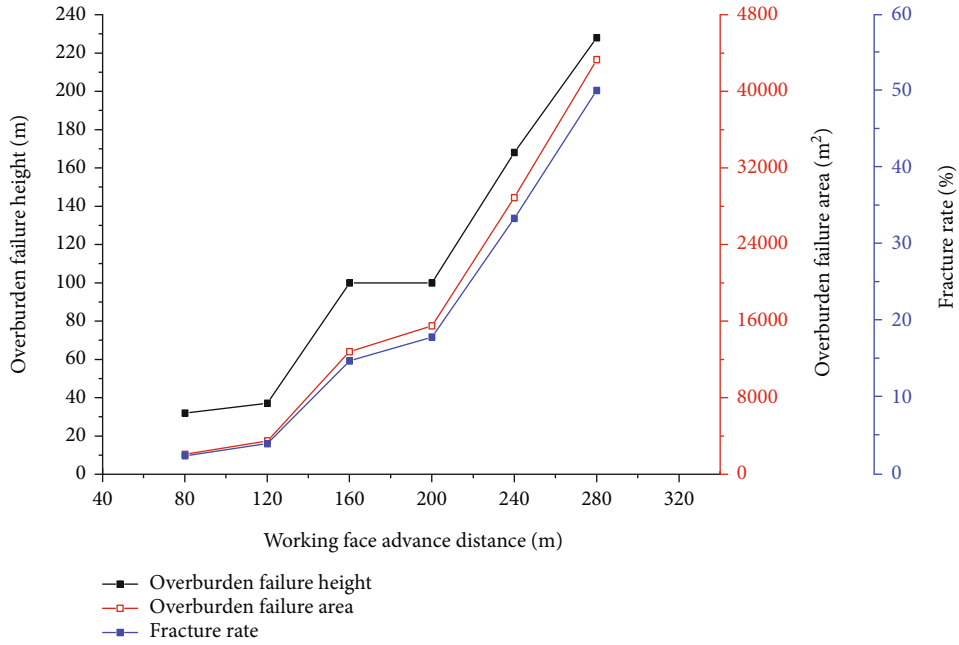

Figure 11: Overburden migration failure fracture evolution curve.

Table 3: The width and height of overburden fracture.

Width (m)	Overburden failure height (m)	Overburden failure area (m^2)	R_f (%)
80	32	2080	2.4
120	37	3478	4.0
160	100	12800	14.8
200	100	15500	17.9
240	168	28896	33.4
280	228	43320	50.1

of loading rate, the tensile-shear mixed failure cracks and shear rupture lines increase, and the shear cracks are positively correlated with the loading rate.

4.2. Overburden Fracture Evolution Law. As shown in Figure 11, with the advancement of the working face, the overburden collapsed trapezoidal boundary morphology evolution characteristics, the overburden collapsed to the goaf, and the overburden collapsed alternately with symmetrical and asymmetrical trapezoids. In the symmetrical trapezoidal evolution stage, the overburden collapsed in a large area, and the fracture height of the trapezoid increased. In the asymmetrical trapezoidal evolution stage, the overburden broke locally, and the increase in the height of the trapezoidal fracture was lower. The damage can be used to describe the random characteristics of the development direction of the overburden fracture [6, 42, 43]. This defines that the fracture rate R_f can be formulated as follows:

$$\mathrm{R_f} = \frac{S_f}{S_a}, \tag{2}$$

where S_f is the total area of fractures and S_a is the total area of research area.

As the working face advances, the fracture height and fracture rate of the overlying rock will increase. Table 3 shows the value of overburden failure height, overburden failure area, and fracture rate. As shown in Figure 12, the initial weighting interval of the main roof of the working face is 54 m, the periodic weighting interval is 12.75~28 m, and the average periodic weighting interval is 22 m. Since the Shendong mining area is currently mainly under shallow coal seam and high-intensity mining conditions, the overburden fracture zone in this area is higher than the thickness of the bedrock, and the ground has collapsed pits, ground cracks, and step sinking damage. There is no overburden damage "three-zone" height, only overburden damage "two zones or one zone" height [44, 45]. The overburden collapse of the 12401 working face only has the caving zone and the fracture zone, the height of the caving zone is 60 m, and the fracture zone is 168 m. Periodic breakage of the key stratum causes the overburden and the ground to sink; the maximum ground subsidence is 5 m. When the working face was excavated from 120 m to 160 m, the height of the overburden fracture did not increase, but the damage range and the fracture rate of the overburden fractures increased, indicating that new fractures developed and expanded laterally during this process. In this process, the fractures are developed and expanded, compaction and new fractures are generated, and the fractures develop to the ground. The fully mining angle of the overburden is basically symmetrical, with an open cut of 61° and a stop mining line of 65°.

4.3. Evolution Law of Temperature Field in Overburden Fracture. In the previous experimental studies, infrared radiation monitoring methods were basically used. Because coal and rock samples are deformed and destroyed under loading

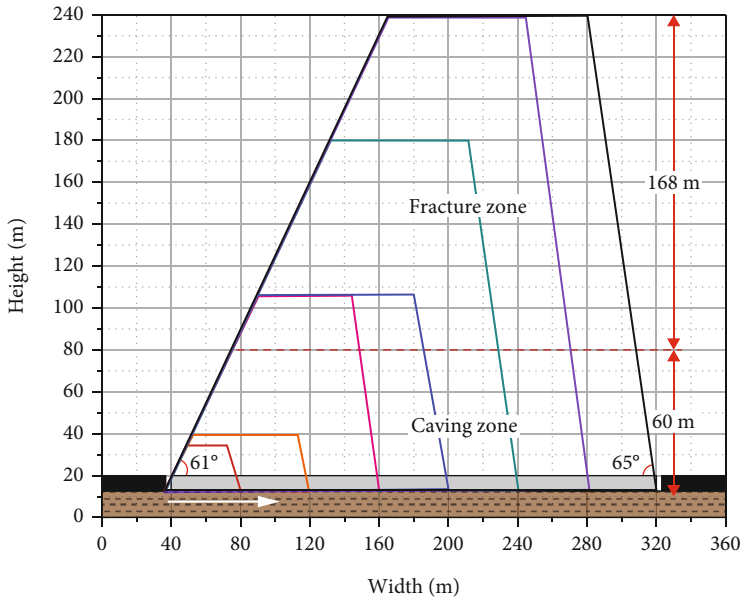

Figure 12: Evolution characteristics of overburden migration failure fracture range.

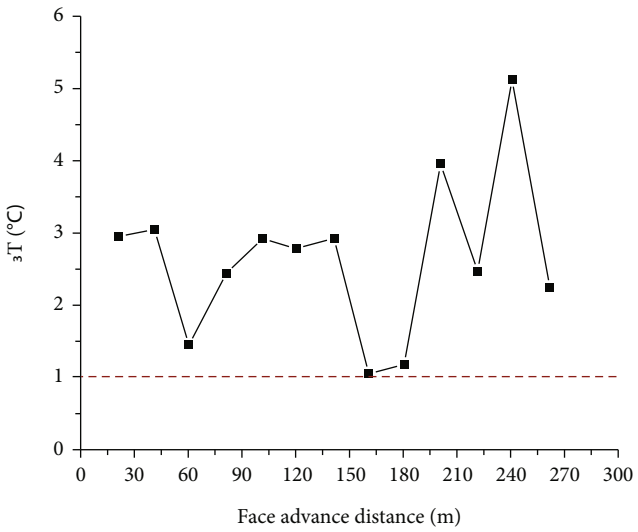

Figure 13: Evolution curve of temperature difference of overburden migration failure fracture.

conditions, they will be accompanied by changes in surface temperature radiation values. Therefore, through temperature field analysis, a quantitative description of the evolutionary law of coal and rock damage can be obtained [46–48]. Therefore, this paper uses infrared monitoring methods to monitor similar simulations. According to the above-mentioned infrared images of similar models under different excavation distances, the temperature of the fracture and the overburden were extracted, respectively, and the average value was calculated. The temperature difference between the fracture and the overburden calculated based on the average value is shown in Figure 13. As the working face advances, the temperature difference between the fracture and the overburden can be divided into two stages. The first stage is when the working face advances from 50 m to 140 m, the roof collapses directly, the fracture is developed in a small range, and the temperature difference is 3°C. The second stage is when the working face advances from 160 m to 280 m, as the working face advances, the main roof periodically breaks, the expansion range of the cracks continues to increase, and the temperature difference is large. In the fracture compaction zone, the fluidity of indoor air in the fracture is relatively small, and the temperature is relatively low, while in the separation fracture zone, the fluidity of the indoor air is relatively high, and the temperature is relatively high, which leads to a large change in the temperature difference at this stage. In the end, during the entire mining process, the temperature difference in the first stage is about 3°C, the maximum temperature difference in the second stage can reach more than 5°C, and the lowest value is about 1°C. Therefore, the temperature difference between the fracture and the overburden value is ≥1°C, which can be used as a threshold for judging the development range of overburden fracture in similar simulation experiments.

5. Conclusions

Based on basic experiments and physical similarity simulations, the effects of hydraulic coupling on mechanical deformation characteristics of shallow coal seam in western mining area are concluded as follows:

(1) The results show that under the loading rate range of 0.5~5 mm/min, the compressive strength of sandstone increases with the loading rate. With the increase of loading rate, the tensile-shear mixed failure cracks and shear rupture lines increase, and the shear cracks are positively correlated with the loading rate. The shorter the duration of the rock sample being loaded and damaged, the fewer the acoustic

emission events. Therefore, the mining speed affects the degree of fracture development in the overburden

(2) The first weighting step of the main roof of the working face is 54 m, the periodic weighting step is 12.75~28 m, and the average periodic weighting step is 22 m. There are only caving zone and fractured zone in the overburden of working face; the height of caving zone and fractured zone is 60 m and 168 m. The fully mining angle of the overburden is basically symmetrical, with an open cut of 61° and a stop line of 65°. When the working face advances 280 m, the fracture is developed to the ground, and the maximum ground subsidence is 5 m

(3) During the excavation of the working face, the temperature difference between the fracture and the overburden is obvious. Therefore, the temperature difference between the fracture and the overburden value is ≥1°C, which can be used as a threshold for judging the development range of overburden fracture in similar simulation experiments

Data Availability

The data used to support the findings of this study are available from the corresponding author upon request.

Conflicts of Interest

The authors declare that they have no conflict of interests.

Acknowledgments

This work was supported by the National Natural Science Foundation of China (nos. U1910206, 51874312, and 51861145403), Major Scientific and Technological Innovation Project of Shandong Province (no. 2019SDZY01), and Science and Technology Project of Inner Mongolia Autonomous Region (no. 2019GG140). These sources of support are gratefully acknowledged.

References

[1] K. A. N. G. Hongpu, "Spatial scale analysis on coal mining and strata control technologies," *Journal of Mining and Strata Control Engineering*, vol. 2, no. 2, pp. 5–30, 2020.

[2] W. B. K. A. N. G. Hongpu and X. U. Gang, "Forty years development and prospects of underground coal mining and strata control technologies in China," *Journal of Mining and Strata Control Engineering*, vol. 1, no. 1, p. 013501, 2019.

[3] D. Zhang, G. Fan, L. Ma, and X. Wang, "Aquifer protection during longwall mining of shallow coal seams: a case study in the Shendong coalfield of China," *International Journal of Coal Geology*, vol. 86, no. 2–3, pp. 190–196, 2011.

[4] D. Zhang, G. Fan, Y. Liu, and L. Ma, "Field trials of aquifer protection in longwall mining of shallow coal seams in China," *International Journal of Rock Mechanics and Mining Sciences*, vol. 47, no. 6, pp. 908–914, 2010.

[5] Z. Song, Y. Wang, H. Konietzky, and X. Cai, "Mechanical behavior of marble exposed to freeze-thaw-fatigue loading," *International Journal of Rock Mechanics and Mining Sciences*, vol. 138, p. 104648, 2021.

[6] C. Wang, N. Zhang, Y. Han, Z. Xiong, and D. Qian, "Experiment research on overburden mining-induced fracture evolution and its fractal characteristics in ascending mining," *Arabian Journal of Geosciences*, vol. 8, no. 1, pp. 13–21, 2015.

[7] W. Yan, H. Dai, and J. Chen, "Surface crack and sand inrush disaster induced by high-strength mining: example from the Shendong coal field, China," *Geosciences Journal*, vol. 22, no. 2, pp. 347–357, 2018.

[8] C. Liu, H. Li, and H. Mitri, "Effect of strata conditions on shield pressure and surface subsidence at a longwall top coal caving working face," *Rock Mechanics and Rock Engineering*, vol. 52, no. 5, pp. 1523–1537, 2019.

[9] J. C. Wang, Z. H. Wang, and S. L. Yang, "Stress analysis of longwall top-coal caving face adjacent to the gob," *International Journal of Mining, Reclamation and Environment*, vol. 34, no. 7, pp. 476–497, 2020.

[10] W. Ren, C. Guo, Z. Peng, and Y. Wang, "Model experimental research on deformation and subsidence characteristics of ground and wall rock due to mining under thick overlying terrane," *International Journal of Rock Mechanics and Mining Sciences*, vol. 47, no. 4, pp. 614–624, 2010.

[11] Z. L. Yang, "Stability of nearly horizontal roof strata in shallow seam longwall mining," *International Journal of Rock Mechanics and Mining Sciences*, vol. 47, no. 4, pp. 672–677, 2010.

[12] N. Jiang and J. Ma, "Modeling study on the influence of the strip filling mining sequence on mining-induced failure," *Energy Science & Engineering*, vol. 8, no. 6, pp. 2239–2255, 2020.

[13] C. Zhu, Y. Yuan, C. Yuan, Z. Chen, and S. Wang, "Study on the structural forms of the key strata in the overburden of a stope during periodic weighting and the reasonable working resistance of the support," *Energy Science & Engineering*, vol. 8, no. 7, pp. 2599–2620, 2020.

[14] J. Cheng, Z. Wang, and W. Lu, "Subsurface strata failure and movement based for improving gas emission control : model development and application," *Energy Science and Engineering*, vol. 2, pp. 3285–3302, 2020.

[15] G. Wang, M. Wu, R. Wang, H. Xu, and X. Song, "Height of the mining-induced fractured zone above a coal face," *Engineering Geology*, vol. 216, pp. 140–152, 2017.

[16] X. Shi, Y. Zhao, S. Gong, W. Wang, and W. Yao, "Co-effects of bedding planes and loading condition on mode-I fracture toughness of anisotropic rocks," *Theoretical and Applied Fracture Mechanics*, vol. 117, p. 103158, 2021.

[17] Z. Song, T. Frühwirt, and H. Konietzky, "Inhomogeneous mechanical behaviour of concrete subjected to monotonic and cyclic loading," *International Journal of Fatigue*, vol. 132, p. 105383, 2020.

[18] Y. Xu, K. Wu, Z. Bai, and Z. Hu, "Theoretical analysis of the secondary development of mining-induced surface cracks in the Ordos region," *Environmental Earth Sciences*, vol. 76, no. 20, pp. 1–9, 2017.

[19] J. Xu, J. Peng, and H. An, "Experimental study on Su-Xi-Chang earth fissures induced by repeated groundwater pumping and impounding," *Geomatics, Natural Hazards and Risk*, vol. 10, no. 1, pp. 2051–2068, 2019.

[20] J. Cao, Q. Huang, and L. Guo, "Subsidence prediction of overburden strata and ground surface in shallow coal seam mining," *Scientific Reports*, vol. 11, no. 1, pp. 1–12, 2021.

[21] Q. F. Hu, X. M. Cui, W. K. Liu, T. J. Ma, and H. R. Geng, "Law of overburden and surface movement and deformation due to mining super thick coal seam," *Journal of Mining and Strata Control Engineering*, vol. 2, no. 2, p. 023021, 2020.

[22] C. Chen, Z. Hu, J. Wang, and J. Jia, "Dynamic surface subsidence characteristics due to super-large working face in fragile-ecological mining areas: a case study in Shendong coalfield, China," *Advances in Civil Engineering*, vol. 2019, 16 pages, 2019.

[23] W. Wang, "Study on the movement characteristics of the overlying stratum and surrounding rock control in ultraclose coal seams : a case study," *Energy Science & Engineering*, vol. 8, no. 4, pp. 1231–1246, 2020.

[24] S. Bhowmick, S. Nagarajaiah, and A. Veeraraghavan, "Vision and deep learning-based algorithms to detect and quantify cracks on concrete surfaces from UAV videos," *Sensors (Switzerland)*, vol. 20, no. 21, article 6299, 2020.

[25] X. He, Y. Zhao, C. Zhang, and P. Han, "A model to estimate the height of the water-conducting fracture zone for longwall panels in Western China," *Mine Water and the Environment*, vol. 39, no. 4, pp. 823–838, 2020.

[26] Y. Zhao, B. Sun, S. Liu et al., "Identification of mining induced ground fissures using UAV and infrared thermal imager: temperature variation and fissure evolution," *ISPRS Journal of Photogrammetry and Remote Sensing*, vol. 180, pp. 45–64, 2021.

[27] X. Wang, W. Zhu, J. Xu, H. Han, and X. Fu, "Mechanism of overlying strata structure instability during mining below unconsolidated confined aquifer and disaster prevention," *Applied Sciences*, vol. 11, no. 4, article 1778, 2021.

[28] X. F. Lv, H. Y. Zhou, A. W. Wang, C. Feng, and X. C. Xiao, "Characteristics of stress transfer and progressive fracture in overlying strata due to mining-induced disturbances," *Advances in Civil Engineering*, vol. 2018, 13 pages, 2018.

[29] L. F. Li, X. H. Zhang, H. L. Deng, and L. P. Han, "Mechanical properties and energy evolution of sandstone subjected to uniaxial compression with different loading rates," *Journal of Mining and Strata Control Engineering*, vol. 2, no. 4, p. 043037, 2020.

[30] H. Wang, R. Shi, C. Lu, Y. Jiang, D. Deng, and D. Zhang, "Investigation of sudden faults instability induced by coal mining," *Safety Science*, vol. 115, pp. 256–264, 2019.

[31] T. Liang, X. Liu, S. Wang, E. Wang, and Q. Li, "Study on the fractal characteristics of fracture network evolution induced by mining," *Advances in Civil Engineering*, vol. 2018, 13 pages, 2018.

[32] Z. Meng, X. Shi, and G. Li, "Deformation , failure and permeability of coal-bearing strata during longwall mining," *Engineering Geology*, vol. 208, pp. 69–80, 2016.

[33] C. Pan and B. Yu, "Determination of the key parameters of high-position hard roofs for vertical-well stratified fracturing to release strong ground pressure behavior in extra-thick coal seam mining," *Energy Science and Engineering*, vol. 8, no. 6, pp. 2216–2238, 2020.

[34] J. Wen, W. Cheng, L. Chen, S. Shi, and Z. Wen, "A study of the dynamic movement rule of overlying strata combinations using a short-wall continuous mining and full-caving method," *Energy Science and Engineering*, vol. 7, no. 6, pp. 2984–3004, 2019.

[35] H. Yang, Z. Liu, D. Zhu, W. Yang, D. Zhao, and W. Wang, "Study on the fractal characteristics of coal body fissure development and the law of coalbed methane migration of around the stope," *Geofluids*, vol. 2020, no. 6, p. 15, 2020.

[36] L. M. Dou, J. He, A. Y. Cao, S. Y. Gong, and W. Cai, "Rock burst prevention methods based on theory of dynamic and static combined load induced in coal mine," *Journal of China Coal Society*, vol. 40, no. 7, pp. 1469–1476, 2015.

[37] X. Shi, W. Yao, D. Liu, K. Xia, T. Tang, and Y. Shi, "Experimental study of the dynamic fracture toughness of anisotropic black shale using notched semi-circular bend specimens," *Engineering Fracture Mechanics*, vol. 205, pp. 136–151, 2019.

[38] Y. Wang, Y. F. Yi, C. H. Li, and J. Q. Han, "Anisotropic fracture and energy characteristics of a Tibet marble exposed to multi-level constant-amplitude MLCA cyclic loads: a lab-scale testing," *Engineering Fracture Mechanics*, vol. 244, p. 107550, 2021.

[39] Z. Song, H. Konietzky, and M. Herbst, "Bonded-particle model-based simulation of artificial rock subjected to cyclic loading," *Acta Geotechnica*, vol. 14, no. 4, pp. 955–971, 2019.

[40] D. Xue, Z. Zhang, C. Chen et al., "Spatial correlation-based characterization of acoustic emission signal-cloud in a granite sample by a cube clustering approach," *International Journal of Mining Science and Technology*, vol. 31, no. 4, pp. 535–551, 2021.

[41] M. Gao, J. Xie, Y. Gao et al., "Mechanical behavior of coal under different mining rates: a case study from laboratory experiments to field testing," *International Journal of Mining Science and Technology*, vol. 31, no. 5, pp. 825–841, 2021.

[42] Y. Wang, B. Zhang, B. Li, and C. H. Li, "A strain-based fatigue damage model for naturally fractured marble subjected to freeze-thaw and uniaxial cyclic loads," *International Journal of Damage Mechanics*, vol. 30, no. 10, pp. 1594–1616, 2021.

[43] P. Xiao and H. Lin, "The effects of key rock layer fracturing on gas extraction during coal mining over a large height," *Energy Science and Engineering*, vol. 2021, pp. 520–534, 2021.

[44] C. Ji, Y. Yang, X. Guo, T. Kang, and Z. Guo, "Influence law of interbedded strata and their collapse on the mining of extremely thick coal seam under goaf," *Advances in Civil Engineering*, vol. 2019, 11 pages, 2019.

[45] X. He, Y. Zhao, K. Yang, C. Zhang, and P. Han, "Development and formation of ground fissures induced by an ultra large mining height longwall panel in Shendong mining area," *Bulletin of Engineering Geology and the Environment*, vol. 80, no. 10, pp. 7879–7898, 2021.

[46] H. Sun, L. Ma, N. Adeleke, and Y. Zhang, "Background thermal noise correction methodology for average infrared radiation temperature of coal under uniaxial loading," *Infrared Physics and Technology*, vol. 81, pp. 157–165, 2017.

[47] L. Ma and H. Sun, "Spatial-temporal infrared radiation precursors of coal failure under uniaxial compressive loading," *Infrared Physics and Technology*, vol. 93, pp. 144–153, 2018.

[48] L. Wu, S. Liu, Y. Wu, and H. Wu, "Changes in infrared radiation with rock deformation," *International Journal of Rock Mechanics and Mining Sciences*, vol. 39, no. 6, pp. 825–831, 2002.